Exploring metal-free ionic covalent organic framework nanosheets as efficient OER electrocatalysts via cationic-π interactions

Rui Wang, Ziqi Zhang, Jinquan Suo, Li Liao, Leibo Li, Zhuochen Yu, Heng Zhang, Valentin Valtchev, Shilun Qiu, Qianrong Fang

Exploring Metal-Free Ionic Covalent Organic Framework Nanosheets as Efficient OER Electrocatalysts via Cationic-π Interactions

*Rui Wang, Ziqi Zhang, Jinquan Suo, Li Liao, Leibo Li, Zhuochen Yu, Heng zhang, Valentin Valtchev, Shilun Qiu, and Qianrong Fang**

R. Wang, Z. Zhang, J. Suo, L. Liao, H. Zhang, Prof. S. Qiu, Prof. Q. Fang
State Key Laboratory of Inorganic Synthesis and Preparative Chemistry, Jilin University, Changchun 130012, R. P. China
L. Li
Key Laboratory of High Performance Plastics, Ministry of Education, Jilin University, Changchun 130012, P. R. China
Z. Yu
State Key Laboratory of Supramolecular Structure and Materials, Jilin University, Changchun 130012, P. R. China
Prof. V. Valtchev
Qingdao Institute of Bioenergy and Bioprocess Technology, Chinese Academy of Sciences, Qingdao 266101, P. R. China; Normandie Univ, ENSICAEN, UNICAEN, CNRS, Laboratoire Catalyse et Spectrochimie, 14050 Caen, France

Corresponding Author

Qianrong Fang: qrfang@jlu.edu.cn

Abstract

Metal-free electrocatalysts play a crucial role in enabling practical water splitting for future clean energy production by facilitating the oxygen evolution reaction (OER). However, the preparation of such electrocatalysts presents significant challenges due to the limitations of the kinetically sluggish anodic half-cell reaction, which restricts the attainment of high energy inputs. In this study, we present a metal- and pyrolysis-free ionic covalent organic framework (COF) nanosheet, denoted as JUC-627-NS, and investigate its potential as an efficient electrocatalyst for OER by introducing cationic-π interactions. Notably, through the utilization of positively charged JUC-627-NS as cationic donors and π-conjugated graphene as electron donors for the first time, the JUC-627-NS@G-2 composite exhibits an exceptional ultralow overpotential of 275 mV at a current density of 10 mA cm^{-2}, ranking among the top-performing metal- and pyrolysis-free electrocatalysts reported thus far. Combining theoretical calculations with in-situ infrared spectroscopy, we validate that the imidazolium salt moiety of JUC-627-NS serves as the active center of the electrocatalyst, while the robust cation-π interaction within the complex brings the reaction site closer to graphene, acting as a conductive agent. These findings highlight a novel strategy for advancing the development of metal-free OER electrocatalysts based on ionic COF materials, with promising applications in energy conversion and storage devices.

Keywords

Covalent Organic Framework, Nanosheet, Metal-free Electrocatalyst, Oxygen Evolution Reaction, Cation-π Interaction

1. Introduction

Over the past few decades, hydrogen has emerged as a clean and promising energy carrier, offering a potential solution to the energy crisis and environmental pollution caused by fossil fuels. [1,2] Electrocatalytic water splitting has emerged as a prospective method for hydrogen production. However, the oxygen evolution reaction (OER) has been identified as a bottleneck in efficient water splitting due to its high energy requirements. The limited energy conversion efficiency is attributed to the kinetically slow anodic half-cell reaction, which involves the transfer of four electrons. [3,4] Although noble transition metal oxides, such as RuO_2 and IrO_2, have demonstrated effectiveness as electrocatalysts for OER, their large-scale application is hindered by their scarcity in nature and associated environmental concerns regarding extraction processes. [5-7] In recent years, metal-free materials have gained attention as they offer environmental friendliness and abundant resources for electrocatalytic OER.[8,9] Notably, Zhao et al. discovered a highly efficient metal-free electrocatalyst for OER in 2013, showcasing an overpotential of 380 mV at a current density of 10 mA cm^{-2}, closing to commercial IrO_2 catalyst (~320 mV).[10] Similarly, Peng et al. developed a metal-free mesoporous N-doped carbon through wood pyrolysis as an OER catalyst, exhibiting an overpotential of 380 mV at a current density of 10 mA cm^{-2}.[11] Additionally, several metal-free carbon-based materials have demonstrated comparable OER performance to noble-metal-containing benchmarks. However, these materials often require pyrolysis, resulting in unpredictability and poorly defined active sites, limiting the understanding of structure-activity relationships.[3,12] Therefore, the development of efficient OER catalysts that are both metal-free and pyrolysis-free with well-defined active sites and tunable structures, remains an urgent priority.

Covalent organic frameworks (COFs) have garnered significant interest as nonmetallic nanomaterials due to their tunable structures and excellent

stability. [13-18] However, the number of COFs reported as metal-free catalysts for the OER remains limited. For example, Zhang et al. developed a novel phenazine-linked 2D COF with exceptional OER activity, achieving an overpotential of 349 mV at 10 mA cm^{-2}.[19] Likewise, Bhaumik et al. reported a metal-free thiadiazole-based COF exhibiting remarkable OER performance, including an onset potential of 270 mV and an overpotential of 320 mV at a current density of 10 mA cm^{-2}.[20] Nonetheless, due to the inherently low conductivity of COFs, additional carbon materials were introduced to enhance electrical conductivity.[21,22] Moreover, the accumulation of COF in the catalyst ink due to π-π interactions hindered full exposure of the reaction sites, while the conductive particles' agglomeration limited their effectiveness in promoting conductivity.[23,24] Introducing an interaction force between the active substance and the conductive particles was found to be beneficial in inhibiting agglomeration and enhancing electron transfer efficiency.[25,26] Among these interaction forces, cation-π interactions, formed when graphene serves as the π electron donor, have attracted extensive attention in electrochemistry due to their remarkable strength.[27,28] Interestingly, although metal-free ionic COF nanosheets offer the potential to improve cation-π interactions between the active framewrok and the conductive agent, their application as electrocatalysts for OER remains unexplored.

Herein, we present a metal- and pyrolysis-free ionic COF nanosheet, named JUC-627-NS, and firstly investigate its potential as an electrocatalyst for the OER through the utilization of cation-π interactions. By introducing the interaction between COF nanosheets and graphene, JUC-627-NS@G-2 demonstrates a remarkably low OER overpotential of only 275 mV at a current density of 10 mA cm^{-2}. To the best of our knowledge, this value stands as one of the lowest among all previously reported metal- and pyrolysis-free electrocatalytic materials, including COFs, hydrogen-bonded organic frameworks (HOFs), and pyrolysis-free carbon materials. Furthermore, it

surpasses the performance of commercial noble metal-based catalysts such as Pt/C, IrO_2, and RuO_2. Additionally, through a combination of experimental results and theoretical analysis, we elucidate that the cation-π interaction between JUC-627-NS and graphene facilitates smooth conductive pathways and excellent charge and electrolyte transfer channels, thereby contributing to its exceptional OER activity. Consequently, this work presents a novel approach to the development of efficient metal-free OER electrocatalysts by utilizing ionic COF matrix composites based on cation-π interactions.

2. Experimental Section

2.1. Synthesis of JUC-626

[1,1'-Biphenyl]-4,4'-dicarboxylic acid, dihydrazide (20.27 mg) and 2,4,6-trihydroxy-1,3,5-ben-zenetricarboxaldehyde (10.51 mg) were loaded into a pyrex tube, and 1.4 mL mesitylene, 0.6 mL dimethylacetamide and 0.2 mL of acetic acid (6 M) was added. The liquid nitrogen bath was used to flashly freeze the pyrex tube, which was evacuated to an interior pressure of ca. 19.0 mbar and flame-sealed, decreasing the whole length by ca. 10.0 cm. The tube was placed in an oven at 85 °C for 7 d after the temperature increasing to room temperature. The resulting precipitate was filtered, exhaustively washed with acetone for 5 times. The obtained powder was immersed in anhydrous acetone, and the solvent was exchanged with fresh acetone for several times. The sample was then transferred to vacuum chamber and evacuated to 20 mTorr under room temperature, yielding white powder for N_2 adsorption measurements.

2.2. Synthesis of JUC-627

1-((4,4'-di(hydrazinecarbonyl)-[1,1'-biphenyl]-2-yl) methyl)- 3-ethyl-1H -imidazol-3- bromi dedium (20.6 mg) and 2,4,6-Trihydroxy-1,3,5-ben--zenetricarboxaldehyde (6.3 mg) were loaded into a Pyrex tube, and 1.8 mL

mesitylene, 0.2 mL dimethylacetamide and 0.2 mL of acetic acid (6 M) was added. The liquid nitrogen bath was used to flashly freeze the pyrex tube, which was evacuated to an interior pressure of ca. 19.0 mbar and flame-sealed, decreasing the whole length by ca. 10.0 cm. The tube was placed in an oven at 80 °C for 7 d after the temperature increasing to room temperature. The resulting precipitate was filtered, exhaustively washed with acetone for 5 times. The obtained powder was immersed in anhydrous acetone, and the solvent was exchanged with fresh acetone for several times. The sample was then transferred to vacuum chamber and evacuated to 20 mTorr under room temperature, yielding white powder for N_2 adsorption measurements.

2.3. Synthesis of COF nanosheets

JUC-626 was placed in a mortar and ground for 40 mins. The powder was collected and milled in a ball mill at 6000 rpm for 20 mins. Then the powder was collected and dispersed in ethanol at a concentration of 10 mg/mL, sonicated for 18 hours, and the supernatant was collected after standing, and dried to obtain JUC-626-NS. JUC-627-NS were obtained in the same way.

2.4. Synthesis of COF nanosheet and graphene complexes

5 mg of JUC-626-NS or JUC-627-NS and different proportions of graphene 5.0 mg, 10.0 mg, 15.0 mg were added to the mortar grinding 20 mins. After that, remove the complex and add it to the ampoule, adding 0.8 mL of DMAC. The liquid nitrogen bath was used to flashly freeze the pyrex tube, which was evacuated to an interior pressure of ca. 19.0 mbar and flame-sealed, decreasing the whole length by ca. 8.0 cm. The tube was placed in an oven at 80 °C for 3 d after the temperature increasing to room temperature. The resulting precipitate was filtered, exhaustively washed with acetone for 5 times. The obtained powder was immersed in anhydrous acetone, and the solvent was exchanged with fresh acetone for several times. The sample was then

transferred to vacuum chamber and evacuated to 20 mTorr under room temperature, yielding white powder for N_2 adsorption measurements. The products were named JUC-626-NS@G-1 or JUC-627-NS@G-1 (5.0 mg), JUC-626-NS@G-2 or JUC-627-NS@G-2 (10.0 mg), JUC-626-NS@G-3 or JUC-627-NS@G-3 (15.0 mg).

3. Results

3.1. Synthesis and characterizations of COFs

The implementation of the metal-free ionic COF strategy involved the design of a hydrazide-based building unit functionalized with a quaternary ammonium (QA, an ionic salt) group, namely 1-((4,4'-di(hydrazinecarbonyl)-[1,1'-biphenyl]-2-yl)methyl)-3-ethyl-1H-imidazol-3-bromidedium (DBMEI, Scheme 1). The condensation of DBMEI with 2,4,6-trihydroxy-1,3,5-benzenetricarboxaldehyde (TP) resulted in an expanded [2+3] connected network called JUC-627. Typically, JUC-627 was synthesized via a solvothermal reaction of TP and DBMEI in a mixture of N, N-dimethylacetamide (DMAC) and mesitylene (Mes) in the presence of 6 M acetic acid (AcOH) at 80 °C for 7 days (see the Supporting Information for the synthesis method). As a comparison, a metal-free neutral counterpart named JUC-626 was also synthesized using [1,1′-biphenyl]-4,4′-dicarboxylicacid dihydrazide (BDZ) and TP (see the Supporting Information for the synthesis method).

Fourier transform infrared (FT-IR) spectroscopy revealed peaks at 1274 cm^{-1} for JUC-626 and 1268 cm^{-1} for JUC-627, indicating the emergence of new C-N stretching bands. The presence of the C=C moiety was confirmed by new vibrational peaks at 1574 cm^{-1} for JUC-626 and 1572 cm^{-1} for JUC-627 (see Figures S1 and S2). The successful polymerization of amine and aldehyde groups was evidenced by the disappearance of peaks at 1668 cm^{-1} (C=O band of TP) and 3198 cm^{-1} (N−H band of BDZ or BDMEI).[29,30]

Solid-state ^{13}C cross-polarization/magic-angle spinning (CP/MAS) NMR spectra exhibited peaks at 143 ppm for JUC-626 and 144 ppm for JUC-627, further confirming the presence of the characteristic ethylene-forming carbon (see Figures S3 and S4).[31,32] Notably, the appearance of a peak at 52 ppm indicated the presence of the QA group in JUC-627 after synthesis (see Figure S4).[33] Elemental analysis confirmed the presence of carbon, hydrogen, oxygen, and nitrogen as determined in Table S1. X-ray photoelectron spectroscopy (XPS) was conducted to analyze the chemical composition of JUC-626 and JUC-627, revealing the absence of any metal elements and the presence of carbon (C), oxygen (O), and nitrogen (N) elements in the COFs (see Figures S5a and S6a). The different nitrogen functionalities were confirmed by examining the high-resolution N 1s spectra (see Figures S5c and S6c). In the case of JUC-626, the N 1s spectrum exhibited peaks corresponding to NH-CH_2 (at 399.3 eV) and O=C-NH (at 400.2 eV).[34,35] Similarly, for JUC-627, the N 1s spectrum displayed peaks corresponding to C-N (at 398.6 eV), NH-CH_2 (at 399.4 eV), O=C-NH (at 400.2 eV), and C=N (at 401.3 eV), further confirming the presence of the QA group.[36-38]

Powder X-ray diffraction (PXRD) measurements, along with structural simulations, were carried out to confirm the high crystallinity of JUC-626 and JUC-627. Geometrical energy minimization using Materials Studio based on eclipsed 2D hexagonal close-packed (**hcb**) nets revealed that JUC-626 crystallized in space group $P6\bar{3}/m$ (No. 175, see Table S2), while JUC-627 crystallized in space group $P6\bar{3}$ (No. 174, see Table S3). Both COFs were simulated with AAstacking and AB stacking, respectively, with clear confirmation of the AA stacking mode (see Figures S7 and S8). The corresponding unit cell parameters were calculated as follows: for JUC-626, $a = b = 38.5726$ Å, $c = 3.4267$ Å, $\alpha = \beta = 90°$, and $\gamma = 120$ °; for JUC-627, $a = b = 37.5857$ Å, $c = 3.2267$ Å, $\alpha = \beta = 90°$, and $\gamma = 120°$. The simulated PXRD patterns exhibited excellent agreement with the experimental results.

Additionally, full profile pattern matching (Pawley) refinements were conducted. As shown in Figure 1a, the peaks observed at 2θ = 2.65, 4.58, 7.01, 8.16 and 26.01° for JUC-626 corresponded to the (100), (110), (200), (220) and (001) planes, respectively. Similarly, in the case of JUC-627, the peaks observed at 2θ = 2.71, 4.70, 7.19, 8.44, and 27.69° corresponded to the (100), (110), (200), (220) and (001) planes, respectively (see Figure 1c). The refinement process yielded PXRD patterns that closely matched the experimental ones, with excellent agreement factors (R_{wp} = 5.20% and R_p = 6.58% for JUC-626, R_{wp} = 3.34% and R_p = 4.26% for JUC-627).

The permanent porosity and specific surface areas of JUC-626 and JUC-627 were examined through nitrogen (N_2) adsorption-desorption analysis conducted at 77 K (see Figures S9 and S10). The N_2 adsorption-desorption isotherms displayed a rapid uptake at a low pressure of $P/P_0 < 0.1$, followed by a distinct step at P/P_0 = 0.15 or 0.25. These isotherms exhibited a typical IV pattern, characteristic of mesoporous materials, as described in the literature.[39-42] The Brunauer-Emmett-Teller (BET) surface areas of JUC-626 and JUC-627 were determined to be 398 and 244 $m^2\ g^{-1}$, respectively (see Figures S11 and S12). It is worth noting that the lower BET surface area of JUC-627 can be attributed to the space occupied by the QA group and its comparatively lower crystallinity.[43] The pore size distributions were analyzed using the Barret-Joyner-Halenda (BJH) method, which revealed pore sizes of 38.2 Å for JUC-626 and 30.8 Å for JUC-627, respectively (see Figures S13 and S14). These results were found to align well with the values obtained from the proposed models (40 Å for JUC-626 and 34.6 Å for JUC-627). Additionally, thermalgravimetric analysis (TGA) demonstrated minimal weight loss below 250 °C under N_2 conditions (see Figure S15). Furthermore, JUC-626 and JUC-627 were subjected to various chemical environments for 3 days, including exposure to different organic solvents such as tetrahydrofuran, acetone, and n-hexane. The results indicated that the crystallinity of both

JUC-626 and JUC-627 remained unchanged (see Figures S16 and S17). Moreover, when exposed to a 1 M KOH (aq) solution for 3 days, both COFs exhibited retained crystal and framework structures, showcasing excellent chemical stability for OER (see Figures S18 and S19).

3.2. Synthesis and supramolecular assembly of nanosheets

The exfoliation of layered crystals into nanosheets effectively enhances the number of active sites available for catalytic reactions in 2D materials, as previously reported.[44-46] Therefore, we proceeded to process these materials into nanosheets using the method depicted in Figure S20. Two COFs (see Figures S21 and S22) were initially ground into smaller particles using a mortar, followed by further grinding with a planetary ball mill. Subsequently, ultrasonic waves were employed to exfoliate thematerials into 2D nanosheets. The resulting nanosheets were designated as JUC-626-NS and JUC-627-NS, respectively. Upon obtaining the nanosheets, their PXRD patterns were assessed, revealing the disappearance of peaks after exfoliation, indicating the destruction of the original crystal structure, consistent with previous findings (see Figures S23 and S24).[47,48] Additionally, their FT-IR spectra were examined, and as demonstrated in Figures S25 and S26, the positions of the absorption bands corresponding to the features C=C and C-N remained relatively unchanged, suggesting the preservation of the chemical bonds linking the monomer units. The morphology of the nanosheets was investigated using transmission electron microscopy (TEM, see Figures S29 and S31). The morphology of the nanosheets was further observed by SEM and AFM, which was consistent with those observed by TEM (see Figures S33 and S34). Energy-dispersive spectrometer (EDS) images displayed uniform distribution of C, N, and O atoms in JUC-626-NS and JUC-627-NS (see Figures S30 and S32). For comparison, the TEM observation also captured the intact laminar structure of graphene (see Figure S27), with EDS spectroscopy confirming the presence of only C atoms and no additional

elements (see Figure S28). Moving forward, JUC-626-NS or JUC-627-NS, along with varying proportions of graphene, were assembled using supramolecular interactions, denoted as JUC-626-NS@G-X or JUC-627-NS@G-X, where X = 1, 2, or 3, as depicted in Figure 2g. The morphology of these assemblies is presented in Figures S35-S40. It is evident that JUC-627-NS@G-X exhibits a more homogeneous distribution compared to JUC-626-NS@G-X, which is extremely beneficial for electrocatalytic OER.[49,50]

In order to validate the presence of cation-π interaction between ionic JUC-627-NS and graphene, we conducted Zeta potential measurements on JUC-626-NS, JUC-627-NS, BDZ, and DBMEI. As shown in Figure 2a, the Zeta potential of JUC-627-NS showed a much higher value than that of JUC-626-NS. Meanwhile, the Zeta potential of DBMEI was much higher than that of BDZ, which indicates that the surface of JUC-627-NS carries a large amount of positive charge. To provide further confirmation, quartz crystal microbalance (QCM) analysis was employed to study the robust cation-π interactions between JUC-627-NS and graphene. However, due to the insolubility of COFs, we utilized BDZ and DBMEI as model molecules for these investigations (see Figure 2b). The QCM sensors were coated with graphene and subsequently immersed in varying solutions containing BDZ or DBMEI, enabling the measurement of mass loading. Notably, the interaction between DBMEI and graphene involved both π-π stacking and cation-π interactions, while BDZ and graphene were solely engaged in π-π stacking. Cation-π interactions are known to exhibit considerable strength relative to other non-covalent interactions such as π-π stacking, surpassing them by several magnitudes.[51,52] The QCM results demonstrated significantly higher mass loading value for DBMEI compared to BDZ, serving as evidence for the existence of cation-π interaction between DBMEI and graphene. To gain deeper insights into the interaction between JUC-627-NS and graphene, we

performed calculations to assess the electrostatic potential of the molecular fragments of JUC-627-NS and the junction system formed between JUC-627-NS and graphene, respectively. The results indicated the presence of positive charges surrounding the imidazole ring (see Figures 2c and S41). When the positive charge on the imidazole ring approached the graphene surface, the positive region tended to be in closer proximity to the graphene, thereby establishing a cation-π interaction. Consequently, this led to alterations in the surface electrostatic potential of the imidazole ring (see Figures 2d, 2e, S42-S45). Furthermore, we conducted calculations to determine the crystal orbital overlap population (COOP) between the two nitrogen atoms on the imidazole ring and the carbon atom or graphene. The analysis of COOP provided valuable insights into the bonding characteristics, including bonding and antibonding interactions represented by positive and negative values, respectively. These values indicate the changes in electron density within the interatomic regions due to interactions. Figure 2f illustrates the shifting of electron density in atoms located near the graphene side, indicating the occurrence of cation-π interactions between the molecular fragments and graphene.

3.3. Electrochemical characterization

Building upon the promising results obtained previously, we further investigated the electrocatalytic OER activity of JUC-626-NS and JUC-627-NS through the recording of linear sweep voltammetry (LSV) curves. All LSV plots were presented after iR compensation. The electrocatalytic performance of the JUC-626-NS@G-X series was found to be favorable, as indicated by the potentials ranging from 1.47 to 1.512 V vs. RHE at a current density of 1 mA cm^{-2}, from 1.715 to 1.777 V vs. RHE at a current density of 10 mA cm^{-2}, and from 1.82 to 2.073 V vs. RHE at a current density of 100 mA cm^{-2} (see Table S4 and Figure 3a).

As anticipated, the JUC-627-NS@G-X series exhibited superior electrocatalytic activity compared to JUC-626-NS@G-X, owing to the presence of the nitrogen-rich charged moiety. The JUC-627-NS@G-X series displayed lower potentials, ranging from 1.35 to 1.437 V vs. RHE at a current density of 1 mA cm^{-2}, 1.505 to 1.593 V vs. RHE at a current density of 10 mA cm^{-2}, and 1.67 to 1.788 V vs. RHE at a current density of 100 mA cm^{-2} (see Figure 3b). For comparison purposes, pristine graphene was also prepared for OER tests and relative to JUC-627@G-X, its potentials is 1.930 V at a current density of 10 mA cm^{-2}, demonstrated significantly lower electrocatalytic activity compared to the COF nanosheets combined with graphene (Table S4). This revealed that pristine graphene has limited catalytic activity, and only plays the role of improving the conductivity of the catalyst rather than as an active center (Figure S50).

Additionally, the LSV curves of three commonly used noble metal-basedcatalysts, namely RuO_2 and IrO_2, were also measured (see Figure S46). To gauge electrocatalytic performance, the overpotentials at a current density of 10 mA cm^{-2} (η_{10}) were collected for all samples (see Figure 3c). Notably, JUC-627-NS@G-2 exhibited a significantly high η_{10} of 275 mV vs. RHE, outperforming noble metal-based catalysts, such as IrO_2 (325 mV vs. RHE) and RuO_2 (288 mV vs. RHE). Furthermore, the mass activity of JUC-627-NS@G-2 was calculated to be an impressive value of 243.06 A g^{-1}, surpassing that of Pt/C, IrO_2, and RuO_2, which was 11.76, 66.87, and 242.13 A g^{-1}, respectively (Table S6). Notably, JUC-627-NS@G-2 demonstrated a lower overpotential compared to the electrocatalysts mentioned in Figure 3d and Table S7, including COFs (e.g., C4-SHz COF, 320 mV),[19] HOFs (e.g., S@HOF-H_2BDC, 358 mV),[53] pyrolysis-free carbon materials such as carbon nanotube composites (e.g., PEMAc@CNTs90, 298 mV),[54] graphene composites (e.g., EBP@NG (1:8), 310 mV),[55] C_3N_4 materials (e.g., g-CN1.5, 316 mV),[56] hydrogel materials (e.g., GH-BGQD2, 330 mV),[57] and black

phosphorus materials (e.g., RP-BP/EG-0.5, 328 mV).[58] Consequently, the successful synthesis of metal-free ionic COF nanosheets with exceptionally low overpotential (η_{10} = 275 mV) holds substantial promise for advancing the field of OER electrocatalysis.

The optical bandgap diagrams of JUC-626-NS and JUC-627-NS were determined utilizing the Kubelka-Munk function. A comparison of the two materials revealed that JUC-627-NS exhibited a lower optical bandgap (2.32 eV) as opposed to JUC-626-NS (2.56 eV), as depicted in Figure S47. Furthermore, the highest occupied molecular orbital (HOMO) energy level and the lowest unoccupied molecular orbital (LUMO) energy level were calculated. The LUMO energy level, determined by cyclic voltammetry (CV), was found to be -3.59 eV, while the HOMO energy level was approximately -5.91 eV, indicating the semiconducting properties of JUC-627-NS (see Figures S48 and S49). To assess the reasons for the lower overpotential exhibited by JUC-626 (or 627)-NS@G-2 compared to other ratios, measurements were taken for contact angle and conductivity. Figures S50 and S51 display the initial contact angle of graphene at approximately 40.02°. As the proportion of COFs increases, the contact angle of the nanosheet decreases due to the hydrophilic structure of the hydrazone group.[80,81] The introduction of QA groups results in a smaller contact angle for JUC-627-NS@G-X compared to JUC-626-NS@G-2, owing to the enhanced hydrophilicity of ionic salts. A more hydrophilic structure undoubtedly offers significant advantages in the development of efficient OER electrocatalysts.[59-61] Conversely, the addition of COF nanosheets leads to a decrease in the conductivity of the composite material as the proportion of graphene decreases (see Figure S52). The lower overpotential observed in JUC-626 (or 627)-NS@G-2 compared to other ratios may be attributed to the delicate balance between hydrophilicity and intrinsic conductivity of the catalyst.

Tafel plots were generated based on the LSV measurements to analyze

the correlation between the potential and the logarithm of the current density. JUC-626-NS@G-2 demonstrated a Tafel slope of 137.35 mV decade^{-1} with linear characteristics (see Figure S53), which is lower than both JUC-626-NS@G-1 (237 mV decade^{-1}) and JUC-626@G-3 (214 mV decade^{-1}). While JUC-627-NS@G-2 exhibited a Tafel slope of 132.94 mV decade^{-1}(see Figure S54), which is also lower than both JUC-627-NS@G-1 (156 mV decade^{-1}) and JUC-627@G-3 (164 mV decade^{-1}) and is consistent with that of metal-free catalysts.[62-64] Additionally, electrochemical impedance spectroscopy (EIS) measurements were conducted under OER conditions to evaluate the materials. The results indicated that JUC-627-NS@G-2 had significantly lower interfacial charge transfer resistance compared to JUC-626-NS@G-2 (see Figure 3e). The simulated equivalent circuit diagram based on the EIS results is shown in the inset of Figure 3e. Durability is a crucial aspect for practical applications, thus, the durability of JUC-626-NS@G-2 and JUC-627-NS@G-2 were assessed at a current density of 10 mA cm^{-2} for 12 hours. The corresponding potential−time chronoamperometric responses displayed a minimal potential rise 7% for JUC-626-NS@G-2 and 9% for JUC-627-NS@G-2, indicating excellent stability in alkaline solution (see Figure 3f). The electrochemically active surface areas (ECSAs) of a series of catalysts for OER were determined by measuring the electrochemical double layer capacitance (Cdl) utilizing the CV method, with non-faradic regions ranging from 0.92 to 1.12 V vs. RHE at a scan rate of 10−80 mV s^{-1} in 1 M KOH (see Figures S55 and S56). The Cdl of the JUC-626-NS@G-X series indicated the capacitance ranging from 0.93 to 1.76 mF cm^{-2}. It is clear that the JUC-627-NS@G-X has higher Cdl than the JUC-626-NS@G-X (Figure S57 and Table S5). The JUC-627-NS@G-X series exhibited superior Cdl compared to JUC-626-NS@G-X, which displayed higher Cdl, ranging from 2.97 to 7.36 mF cm^{-2}. Remarkably, the Cdl of JUC-627-NS@G-2 reached 7.36 mF cm^{-2}, four times higher than that of

JUC-626-NS@G-2 (1.76 mF cm^{-2}). In addition, the original JUC-626-NS (0.07 mF cm^{-2}) has a lower Cdl than the JUC-627-NS (0.11 mF cm^{-2}). Due to the lower conductivity, the Cdl of the original nanosheets is lower than that after compounding with graphene. The substantial specific surface area and large pore structure effectively enhance the electrolyte diffusion, enabling more reactant intermediates to accumulate on the electrode surface and ultimately improving the OER performance.[19] The Faraday efficiency of JUC-627-NS@G-2 was also measured, and as shown in Figure S58, the Faraday efficiency remained above 98.6% for one hour. In addition, the XPS after the OER test (Figures S59-S61, S63 and S65) was obtained by further comparing the XPS before the OER test (Figure S5-S6, S59, S62 and S64), no new peaks were observed, indicating that the OER test shift for electron density on the COF was not noticeable before and after. It is worth noting that some new peaks of carbon, oxygen, and fluorine will appear on the spectra after the OER test, which is typical of nifion adhesives.[66]

3.4. Analysis of OER mechanism

The mechanism underlying the OER facilitated by JUC-627-NS is elucidated through computational simulations employing the CP2K simulation package.[65] In Figure 4a, the active sites for metal-free materials are identified as the unconjugated QA group and the carbon atom adjacent to the nitrogen atom.[67] Three potential locations are selected to evaluate the adsorption of OH^- on the surface of JUC-627-NS (see Figures 4a and S66). The C1 site demonstrated the most favorable OH^- adsorption, with an adsorption energy of 2.13 eV (see Figure S67 and Table S8), thus establishing the C1 atom as the active site for the reaction. The catalytic efficiency of the OER process can be determined by calculating the free energy changes of various adsorbed intermediates (i.e., OH*, O*, and OOH*) on the C1 atom of the surface.[68] The distribution of free energies for the OER pathways at U = 0 V and 1.23 V is obtained by analyzing the free energy changes of the adsorbed intermediates

(see Figure 4b). As depicted in Figure 4b, the rate-determining step for JUC-627-NS in the OER process is determined by the highest free energy associated with OH* adsorption. The free energies of OH* adsorption on the surface of JUC-627-NS are determined to be 2.17 eV and 0.94 eV at U = 0 V and 1.23 V, respectively. In-situ FT-IR spectroscopy is employed to further probe the active sites of the catalyst. As shown in Figure S69, the in-situ FT-IR spectra are measured before and during the catalytic process. The peak at 1582 cm^{-1} corresponds to the C=N stretching band[69], indicating a stronger signal during the reaction and confirming the C1 atom as the active site. With time going, the imine bond signal became weaker, and the catalyst activity gradually decreases, which correlates well with the stability of JUC-627-NS@G-2 (see Figure 3f). The decline in activity may be attributed to the prolonged interaction between the oxygen produced and the imidazolium salt, which is not readily removed. The occurrence of ion-dipole interactions is confirmed by the observed blue shift in the in-situ FT-IR spectra as the reaction progresses.[70,71] Furthermore, the in-situ infrared curves of JUC-627 at different voltages were measured as shown in Figure 4c. As the voltage increases, its OER activity increases, and in addition to the original imine bond peak, there is an additional peak of 1708 cm^{-1}, which is considered to be an OOH* intermediate adsorbed by the catalyst. Subsequently, the turnover frequency (TOF) of JUC-627-NS@G-X is calculated to determine its catalytic activity (see Figure S68). Notably, JUC-627-NS@G-2 exhibited a higher TOF value of 0.093 at an overpotential of 300 mV compared to JUC-627-NS@G-1 and JUC-627-NS@G-3.

The influence of graphene in augmenting the catalytic activity of ionic COFs was further investigated. For comparison, LSV curves were measured for JUC-626-NS and JUC-627-NS without being bound to graphene. Given the absence of a conductive agent, these samples exhibited poor OER performance, with the current density of JUC-626-NS and JUC-627-NS

reaching only 10 mA cm^{-2} at 2.26 V and 2.42 V, respectively (see Figure S70). Graphene exhibits exceptional properties in supporting a highly conductive network and facilitating interactions with nanosheets, resulting in improved conductivity and reduced charge transfer resistance (see Figures 3e and S71). The reduction in charge transfer resistance can be attributed to the presence of cationic-π interactions between JUC-627-NS and graphene.[72-74] In order to further investigate this phenomenon, in-situ Raman spectra of graphene, JUC-626-NS@G-2, and JUC-627-NS@G-2 were measured at a current density of 10 mA cm^{-2} (Figure 4d). Interestingly, the Raman spectrum of JUC-627-NS@G-2 displayed a distinct blue shift compared to the original graphene spectrum, indicating the persistent presence of cation-π interactions even at 10 mA cm^{-2}.[75-76] Furthermore, the defect degree of carbon networks in graphene, JUC-626@G-2 and JUC-627@G-2 was calculated according to in-situ Raman spectroscopy. Among them, the carbon network defects of G, JUC-626@G-2 and JUC-627@G-2 were 1.023, 1.002 and 0.995, respectively, indicating that the carbon network basically did not have any defective changes in the process of OER catalysis. In addition, pore defects in catalyst may give rise to the change of the OER. Considering the similar structures of JUC-626 and JUC-627, it is expected that the defects in JUC-627@G-2 and JUC-626@G-2 would be approximately equivalent. However, it is noteworthy that the overpotential of JUC-627@G-2 is considerably lower than that of JUC-626@G-2. This suggests that the superior performance of JUC-627@G-2 can be attributed to the imidazolium salt moiety of JUC-627, which acts as the active center for electrocatalysis, rather than being solely influenced by the presence of defects. This strong cation-π interaction can be attributed to the proximity of the imidazole functional group, located at the C1 atom containing the active site, to graphene. Consequently, this proximity facilitates the transfer of electrons from graphene to the active site, as illustrated in Figure 4e.

4. Conclusions

In summary, we have successfully designed and synthesized JUC-627-NS, an ionic COF nanosheet, without the use of metals or pyrolysis. We have also investigated its potential as an electrocatalyst for the OER by incorporating cationic-π interactions with graphene, which is a novel approach. Interestingly, the composite material JUC-627-NS@G-2, formed by combining positively charged JUC-627-NS as cationic donors and π-conjugated graphene as electron donors, exhibited the lowest overpotential (275 mV at a current density of 10 mA cm^{-2}) among metal-free materials and even commercial noble metal catalysts. Through theoretical calculations and in-situ infrared spectroscopy, we have elucidated that the introduced cation-π interactions with graphene contribute to the superior OER performance observed and we demonstrate that the active site is located on the imidazole salt of JUC-627, but not on graphene, which is introduced only as a conductive particle. This work presents a promising strategy for the development of highly efficient OER electrocatalysts, which can significantly impact the field of energy conversion and storage devices.

CRediT authorship contribution statement

Rui Wang: Investigation, Methodology, Writing, Original draft. Zi-Qi Zhang: Methodology, Data curation. Jin-Quan Suo: Theoretical calculations. Li Liao: Methodology, Data curation. Lei-Bo Li: Investigation, Validation. Zhuo-Chen Yu: Build the model. Heng Zhang: Methodology, Data curation. Valentin Valtchev: Writing – review & editing. Shi-Lun Qiu: Writing – review & editing. Qian-Rong Fang: Conceptualization, Supervision, Project administration, Funding acquisition, Writing – review & editing.

Declaration of Competing Interest

There are no conflicts to declare.

Acknowledgements

This work was supported by National Key R&D Program of China (2022YFB3704900 and 2021YFF0500500), National Natural Science Foundation of China (22025504, 21621001, and 22105082), the SINOPEC Research Institute of Petroleum Processing, "111" project (BP0719036 and B17020), China Postdoctoral Science Foundation (2020TQ0118 and 2020M681034), and the program for JLU Science and Technology Innovative Research Team. V.V., Q.F. and S.Q. acknowledge the collaboration in the Sino-French International Research Network “Zeolites”.

Supporting information

Supplementary data associated with this article can be found in the online version.

References

[1] X. Zou, Y. Zhang, Noble metal-free hydrogen evolution catalysts for water splitting. Chem. Soc. Rev. 44 (2015) 5148-5180.

[2] I. Roger, M. A. Shipman, M. D. Symes, Earth-abundant catalysts for electrochemical and photoelectrochemical water splitting. Nat. Rev. Chem. 1 (2017) 0003.

[3] X. Cui, L. Gao, R. Ma, Z. Wei, C. Lu, Z. Li, Y. Yang, Pyrolysis-free covalent organic framework-based materials for efficient oxygen electrocatalysis. J. Mater. Chem. A 9 (2021) 20985-21004.

[4] M. Gopalakrishnan, A. A. Mohamad, M. T. Nguyen, T. Yonezawa, J. Qin, P. Thamyongkit, A. Somwangthanaroj, S. Kheawhom, Recent advances in oxygen electrocatalysts based on tunable structural polymers. Mater.Today Chem. 23 (2022) 100632-100653.

[5] Q. Shi, C. Zhu, D. Du, Y. Lin, Robust noble metal-based electrocatalysts for oxygen evolution reaction. Chem. Soc. Rev. 48 (2019) 3181-3192.

[6] X. Li, X. Hao, A. Abudulaa, G. Guan, Nanostructured catalysts for electrochemical water splitting: current state and prospects. J. Mater. Chem. A 4 (2016) 11973-12000.

[7] H. Wang, C. Tang, Q. Zhang, A Review of Precious-Metal-Free Bifunctional Oxygen Electrocatalysts: Rational Design and Applications in Zn−Air Batteries. Adv. Funct. Mater. 28 (2018) 1803329.

[8] G. Wu, A. Santandreu, W. Kellogg, S. Gupta, O. Ogoke, H. Zhang, H. Wang, L. Dai, Carbon nanocomposite catalysts for oxygen reduction and evolution reactions: From nitrogen doping to transition-metal addition. Nano Energy 29, (2016), 83-110.

[9] C. Hu, R. Paul, Q. Dai, L. Dai, Carbon-based metal-free electrocatalysts: from oxygen reduction to multifunctional electrocatalysis. Chem. Soc. Rev. 50 (2021) 11785-11843.

[10] Y. Zhao, R. Nakamura, K. Kamiya, S. Nakanishi, K. Hashimoto, Nitrogen-doped carbon nanomaterials as non-metal electrocatalysts for water oxidation. Nat. Commun. 4 (2013) 2390-2396.

[11] X. Peng, L. Zhang, Z. Chen, L. Zhong, D. Zhao, X. Chi, X. Zhao, L. Li, X. Lu, K. Leng, C. Liu, W. Liu, W. Tang, K. P. Loh, Hierarchically porous carbon plates derived from wood as bifunctional ORR/OER electrodes. Adv. Mater., 31 (2019) 1900341.

[12] B. Huang, L. Li, X. Tang, W. Zhai, Y. Hong, T. Hu, K. Yuan, Y. Chen, Pyrolysis-free polymer-based oxygen electrocatalysts. Energy Environ. Sci. 14 (2021) 2789-2808.

[13] A. P. Cote, A. I. Benin, N. W. Ockwig, M. O'Keeffe, A. J. Matzger and O. M. Yaghi, Porous, Crystalline, Covalent Organic Frameworks. Science, 310, (2005) 1166-1170.

[14] X. Chen, K. Geng, R. Liu, K. Tan, Y. Gong, Z. Li, S. Tao, Q. Jiang, D. Jiang, Covalent Organic Frameworks: Chemical Approaches to Designer Structures and Built-In Functions. Angew. Chem. Int. Ed. 59 (2020) 5050-5091.

[15] X. Guan, Q. Fang, Y. Yan, S. Qiu, Functional Regulation and Stability Engineering of Three-Dimensional Covalent Organic Frameworks. Acc. Chem. Res. 14 (2022) 1912-1927.

[16] M. Li, J. Liu, Y. Li, G. Xing, X. Yu, C. Peng, L. Chen, Skeleton Engineering of Isostructural 2D Covalent Organic Frameworks: Orthoquinone Redox-Active Sites Enhanced Energy Storage. CCS Chemistry. 9 (2020) 696-706.

[17] X. Guan, F. Chen, Q. Fang, S. Qiu, Design and applications of three dimensional covalent organic frameworks. Chem. Soc. Rev. 49 (2020) 1357-1384.

[18] Y. Yusran, X. Guan, H. Li, Q. Fang, S. Qiu. Postsynthetic functionalization of covalent organic frameworks. Natl. Sci. Rev. 7 (2020) 170-190.

[19] S. Mondal, B. Mohanty, M. Nurhuda, S. Dalapati, R. Jana, M. Addicoat, A. Datta, B. K. Jena, and A. Bhaumik A Thiadiazole-Based Covalent Organic Framework: A Metal-Free Electrocatalyst toward Oxygen Evolution Reaction. ACS Catal. 10 (2020) 5623-5630.

[20] C. Yang, Z. Yang, H. Dong, N. Sun, Y. Lu, F. Zhang, G. Zhang, Theory-Driven Design and Targeting Synthesis of a Highly-Conjugated

Basal-Plane 2D Covalent Organic Framework for Metal-Free Electrocatalytic OER. ACS Energy Lett. 4 (2019) 2251-2258.

[21] Y. Zhu, S. Jiang, X. Jing, X. Feng, Electrically conductive 2D covalent organic frameworks. Trends Chem. 4 (2022) 128-141.

[22] C. Lin, D. Zhang, Z. Zhao, Z. Xia, Covalent Organic Framework Electrocatalysts for Clean Energy Conversion. Adv. Mater. 30 (2018) 1703646.

[23] M. Xu, J. Li, X. Wu, T. Yu, G. Qin, F. Wang, L. Zhang, K. Li, X. Cheng, The excellent photocatalytic overall water splitting activity of TpPa-1-COF excited via MOF derived FeP-PC and α-Fe_2O_3 dual cocatalysts. Appl. Surf. Sci. 602 (2022) 154371.

[24] S. Zhang, Q. Yang, X. Xu, X. Liu, Q. Li, J. Guo, N. L. Torad, S. M. Alshehri, T. Ahamad, Md. S. A. Hossain, Y. V. Kaneti, Y. Yamauchi, Assembling well-arranged covalent organic frameworks on MOF-derived graphitic carbon for remarkable formaldehyde sensing. Nanoscale, 12 (2020) 15611-15619.

[25] S. Y. Jeong, S. H. Kim, J. T. Han, H. J. Jeong, S. Y. Jeong, G. W. Lee, Highly Concentrated and Conductive Reduced Graphene Oxide Nanosheets by Monovalent Cation–π Interaction: Toward Printed Electronics. Adv. Funct. Mater. 22 (2012) 3307-3314.

[26] W. Wu, A. M. Kirillov, X. Yan, P. Zhou, W. Liu, Y. Tang, Enhanced Separation of Potassium Ions by Spontaneous K^+-Induced Self-Assembly of a Novel Metal–Organic Framework and Excess Specific Cation–π Interactions. Angew. Chem. Int. Ed. 40 (2014) 10649-10653.

[27] Z. Zhen, Z. Li, X. Zhao, Y. Zhong, M. Huang, H. Zhu, Metal-support interaction boosted electrocatalysis of ultrasmall iridium nanoparticles

supported on nitrogen doped graphene for highly efficient water electrolysis in acidic and alkaline media. Nano Energy 62 (2019) 117-126.

[28] M. Cheng, W. Zhang, W. Yuan, Jie Xue, C. Li, S. Hou, Rational Fabrication of MXene / Graphene Oxide Membrane and Its Voltage-Gated Ion Transport Behavior. ACS Sus. Chem. Eng. 9 (2021) 7206-7210.

[29] D. Li, C. Li, L. Zhang, H. Li, L. Zhu, D. Yang, Q. Fang, S. Qiu, X. Yao, Metal-Free Thiophene-Sulfur Covalent Organic Frameworks: Precise and Controllable Synthesis of Catalytic Active Sites for Oxygen Reduction. J. Am. Chem. Soc. 142 (2020) 8104-8108.

[30]F. Chen, X. Guan, H. Li, J. Ding, L. Zhu, B. Tang, V. Valtchev, Y. Yan, S. Qiu, Q. Fang, Three-Dimensional Radical Covalent Organic Frameworks as Highly Efficient and Stable Catalysts for Selective Oxidation of Alcohols. Angew. Chem. Int. Ed. 60 (2021) 22230-22235.

[31] S. Mitra, H. S. Sasmal, T. Kundu, S. Kandambeth, K. Illath, D. D. Díaz, R. Banerjee, Targeted Drug Delivery in Covalent Organic Nanosheets (CONs) via Sequential Postsynthetic Modification. J. Am. Chem. Soc. 139 (2017) 4513-4520.

[32] L. Liao, X. Guan, H. Zheng, Z. Zhang, Y. Liu, H. Li, L. Zhu, S. Qiu, X. Yao, Q. Fang, Three-dimensional microporous and mesoporous covalent organic frameworks based on cubic building units. Chem. Sci. 13 (2022) 9305-9309.

[33] X. He, Y. Yang, H. Wu, G. He, Z. Xu, Y. Kong, L. Cao, B. Shi, Z. Zhang, C. Tongsh, K. Jiao, K. Zhu, Z. Jiang, De novo design of covalent organic framework membranes toward ultrafast anion transport. Adv. Mater. 32 (2020) 2001284.

[34] Y. Li, X. Guo, X. Li, M. Zhang, Z. Jia, Y. Deng, Y. Tian, S. Li, L. Ma, Redox-Active Two-Dimensional Covalent Organic Frameworks (COFs) for Selective Reductive Separation of Valence-Variable, Redox-Sensitive and Long-Lived Radionuclides. Angew. Chem. Int. Ed. 59 (2020) 4168-4175.

[35] S. Yan, X. Guan, H. Li, D. Li, M. Xue, Y. Yan, V. Valtchev, S. Qiu, Q. Fang, Three-dimensional Salphen-based Covalent−Organic Frameworks as Catalytic Antioxidants. J. Am. Chem. Soc. 141 (2019) 2920-2924.

[36] J. Lin, S. Bi, Z. Fan, Z. Fu, Z. Meng, Z. Hou, F. Zhang, A metal-free approach to bipyridinium salt-based conjugated porous polymers with olefin linkages. Polym. Chem. 12 (2021) 1661-1667.

[37] L. Ding, B. Yao, F. Li, S. Shi, N. Huang, H. Yin, Q. Guan, Y. Dong, Ionic liquid-decorated COF and its covalent composite aerogel for selective CO_2 adsorption and catalytic conversion. J. Mater. Chem. A 7 (2019) 4689-4698.

[38] C. He, Q. Wu, M. Mao, Y. Zou, B. Liu, Y. Huang, R. Cao, Multifunctional Gold Nanoparticles@ Imidazolium -Based Cationic Covalent Triazine Frameworks for Efficient Tandem Reactions. CCS Chemietry 2 (2020) 2368-2380.

[39] D. N. Bunck, W. R. Dichtel, Bulk Synthesis of Exfoliated Two-Dimensional Polymers Using Hydrazone-Linked Covalent Organic Frameworks. J. Am. Chem. Soc. 135 (2013) 14952-14955.

[40] W. Liu, X. Li, C. Wang, H. Pan, W. Liu, K. Wang, Q. Zeng, R. Wang, J. Jiang, A Scalable General Synthetic Approach toward Ultrathin Imine Linked Two-Dimensional Covalent Organic Framework Nanosheets for Photocatalytic CO2 Reduction. J. Am. Chem. Soc. 141 (2019) 17431-17440.

[41] Y. Zang, Y. Cheng, Z. Wang, P. Peng, Q. Dong, H. Chen, R. Wang, S. Zang, Ionic covalent organic nanosheet anchoring discrete copper for efficient quasi-homogeneous photocatalytic proton reduction. Appl. Catal. B- Environ. 302 (2022) 120817.

[42]J. Chang, H. Li, J. Zhao, X. Guan, C. Li, G. Yu, V. Valtchev, Y. Yan, S. Qiu, Q. Fang, Tetrathiafulvalene-based covalent organic frameworks for ultrahigh iodine capture. Chem. Sci. 12 (2021) 8452-8457.

[43] J. Wang, J. Zhang, S. B. Peh, G. Liu, T. Kundu, J. Dong, Y. Ying, Y. Qian, D. Zhao,Cobalt-containing covalent organic frameworks for visible light-driven hydrogen evolution. Sci. China Chem. 63 (2020) 192-197.

[44] Y. Kong, X. He, H. Wu, Y. Yang, L. Cao, R. Li, B. Shi, G. He, Y. Liu, Q. Peng, C. Fan, Z. Zhang, Z. Jiang, Tight Covalent Organic Framework Membranes for Efficient Anion Transport via Molecular Precursor Engineering. Angew. Chem. Int. Ed. 60 (2021) 17638-17646.

[45] H. Li, J. Ding, X. Guan, F. Chen, C. Li, L. Zhu, M. Xue, D. Yuan, V. Valtchev, Y. Yan, S. Qiu, Q. Fang, Three-Dimensional Large-Pore Covalent Organic Framework withstp Topology J. Am. Chem. Soc. 142 (2020) 13334-13338.

[46]Y. Liu, J. Ren, Y. Wang, X. Zhu, X. Guan, Z. Wang, Y. Zhou, L. Zhu, S. Qiu, S. Xiao and Q. Fang, A Stable Luminescent Covalent Organic Framework Nanosheet for Sensitive Molecular Recognition. CCS Chemistry (2022) DOI: 10.31635/ccschem.022.202202352.

[47] T. Huang, H. Jiang, John C. Douglin, Y. Chen, S. Yin, J. Zhang, X. Deng, H. Wu, Y. Yin, Dario R. Dekel, Michael D. Guiver, Z. Jiang, Single Solution-Phase Synthesis of Charged Covalent Organic Framework

Nanosheets with High Volume Yield. Angew. Chem. Int. Ed. 62 (2023) e202209306.

[48]J. Wang, N. Li, Y. Xu and H. Pang, Two‐dimensional MOF and COF nanosheets: synthesis and applications in electrochemistry. Chem. Eur. J. 26 (2020) 6402-6422.

[49] F. Zeng, C. Mebrahtu, L. Liao, Anna K. Beine, R. Palkovits, Stability and deactivation of OER electrocatalysts: A review. J. Energy Chem. 69 (2022) 301-329.

[50]H. Jin, B. Ruqia, Y. Park, H. J. Kim, H. Oh, S. Choi, K. Lee, Nanocatalyst Design for Long-Term Operation of Proton/Anion Exchange Membrane Water Electrolysis. Adv. Energy Mater. 11 (2021) 2003188.

[51]S. Mecozzi, A. P. West, D. A. Dougherty, Cation−π Interactions in Simple Aromatics: Electrostatics Provide a Predictive Tool. J. Am. Chem. Soc. 118 (1996) 2307-2308.

[52] G. Zhao, H. Zhu Cation− π interactions in simple aromatics: electrostatics provide a predictive tool. Adv. Mater. 32, (2020)1905756.

[53] J. Wang, L. Zhang, S. Lin, A Porous Hydrogen-Bonded Organic Framework Material for the Sustained Release of Ibuprofen. Z. Anorg. Allg. Chem. 648 (2022) e202200125.

[54]Y. Zhang, X. Fan, J. Jian, D. Yu, Z. Zhang, L. Dai, A general polymer-assisted strategy enables unexpected efficient metal-free oxygen-evolution catalysis on pure carbon nanotubes. Energy Environ. Sci. 10 (2017) 2312-2317.

[55] Z. Yuan, J. Li, M. Yang, Z. Fang, J. Jian, D. Yu, X. Chen, L. Dai, Ultrathin Black Phosphorus-on-Nitrogen Doped Graphene for Efficient Overall Water

Splitting: Dual Modulation Roles of Directional Interfacial Charge Transfer. J. Am. Chem. Soc. 141 (2019) 4972-4979.

[56] B. Z. Desalegn, H. S. Jadhav, J. G. Seo, Highly Efficient g-C_3N_4 Nanorods with Dual Active Sites as an Electrocatalyst for the Oxygen Evolution Reaction. ChemCatChem, 11 (2019) 2870-2878.

[57] T. V. Tam, S. G. Kang, M. H. Kim, S. G. Lee, S. H. Hur, J. S. Chung, W. M. Choi, Novel graphene hydrogel/B‐doped graphene quantum dots composites as trifunctional electrocatalysts for Zn− air batteries and overall water splitting. Adv. Energy Mater. 9 (2019) 1900945.

[58] K. Bai, J. Fan, P. Shi, Y. Min, Q. Xu, Directly ball milling red phosphorus and expended graphite for oxygen evolution reaction. J. Power Sources 456 (2020) 228003.

[59] S. Chen, J. Duan, M. Jaroniec, S. Qiao, Nitrogen and oxygen dual‐doped carbon hydrogel film as a substrate‐free electrode for highly efficient oxygen evolution reaction. Adv. Mater. 26 (2014) 2925-2930.

[60] J. Zhang, L. Dai, Nitrogen, phosphorus, and fluorine tri‐doped graphene as a multifunctional catalyst for self‐powered electrochemical water splitting. Angew. Chem. Int. Ed., 55 (2016) 13296-13300.

[61] Y. Liang, Y. Han, J. Li, J. Wang, D. Liu, Q. Fan, Wettability control in electrocatalyst: A mini review. J. Energy Chem. 2022, 70, 643-655.

[62]Y. Yan, T. He, B. Zhao, K. Qi, H. Liu, B. Xia, Metal/covalent–organic frameworks-based electrocatalysts for water splitting. J. Mater. Chem. A 6 (2018) 15905-15926.

[63] Y. Zhao, J. Zhang, L. Qu, Graphitic Carbon Nitride/Graphene Hybrids as New Active Materials for Energy Conversion and Storag. Chem. Nano Mat. 1 (2015) 298-318.

[64] M. Kuang, G. Zheng, Nanostructured Bifunctional Redox Electrocatalysts. small 12 (2016) 5656-5675.

[65] T. Lu, Q. Chen, Shermo: A general code for calculating molecular thermochemistry properties. Comput. Theor. Chem. 1200 (2021) 113249.

[66] C. Chen, G. Levitin, D. W. Hess, Thomas F. Fuller, XPS investigation of Nafion membrane degradation. J. Power Sources, 169 (2007) 288-295.

[67] T. Ma, S. Dai, M. Jaroniec, S. Qiao, Graphitic carbon nitride nanosheet–carbon nanotube three‐dimensional porous composites as high‐performance oxygen evolution electrocatalysts. Angew. Chem. Int. Ed., 53 (2014) 7281-7285.

[68] S. Nandi, S. K. Singh, D. Mullangi, R. Illathvalappil, L. George, C. P. Vinod, S. Kurungot, R. Vaidhyanathan Low Band Gap Benzimidazole COF Supported Ni3N as Highly Active OER Catalyst. Adv. Energy Mater. 6 (2016) 1601189.

[69] N. A. Noorhisham, D. Amri, A. H. Mohamed, N. Yahaya, N. M. Ahmad, S. Mohamad, S. Kamaruzaman, H. Osman, Characterization techniques for analysis of imidazolium-based ionic liquids and application in polymer preparation: A review. J. Mol. Liq. 326 (2021) 115340.

[70] W. Qiu, G. Chen, H. Zhu, Q. Zhang, S. Zhu, Enhanced stretchability and robustness towards flexible ionotronics via double-network structure and ion-dipole interactions. Chem. Eng. J. 434 (2022) 134752.

[71] P. Shi, Y. Wang, W. W. Tjiu, C. Zhang, T. Liu, Highly Stretchable, Fast Self-Healing, and Waterproof Fluorinated Copolymer Ionogels with Selectively

Enriched Ionic Liquids for Human-Motion Detection. ACS Appl. Mater. Interfaces 13 (2021) 49358-49368.

[72] J. Yin, X. Li, J. Yu, Z. Zhang, J. Zhou, W. Guo, Generating electricity by moving a droplet of ionic liquid along graphene. Nat. Nanotechnol. 9 (2014) 378-383.

[73] W. Fei, C. Shen, S. Zhang, H. Chen, L. Li, W. Guo, Waving potential at volt level by a pair of graphene sheets. Nano Energy 60 (2019) 656-660.

[74] Y. Zhu, W. Cai, R. D. Piner, A. Velamakanni, R. S. Ruoff, Transparent self-assembled films of reduced graphene oxide platelets. Appl. Phys. Lett., 95 (2009) 103104.

[75] C. Xu, L. Yuan, G. Liang, A. Gu, Building a poly(epoxy propylimidazolium ionic liquid)/graphene hybrid through πcation–π interaction for fabricating high-k polymer composites with low dielectric loss and percolation threshold. J. Mater. Chem. C 4 (2016) 3175-3184.

[76] H. Zhang, L. Lyu, Q. Fang, C. Hu, S. Zhan, T. Li, Cation−π structure inducing efficient peroxymonosulfate activation for pollutant degradation over atomically dispersed cobalt bonding graphene-like nanospheres. Appl. Catal. B: Environ. 286 (2021) 119912.

[77] L. Lin, Y. Ni, L. Shang, H. Sun, Q. Zhang, W. Zhang, Z. Yan, Q. Zhao, Jun Chen, Atomic-Level modulation-induced electron redistribution in Co coordination polymers elucidates the oxygen reduction mechanism. ACS Catal. 12 (2022) 7531–7540.

[78] Z. Sun, L. Lin, J. He, D. Ding, T. Wang, J. Li, M. Li, Y. Liu, Y. Li, M. Yuan, B. Huang, H. Li, G. Sun, Regulating the spin state of Fe^{III} enhances the magnetic effect of the molecular catalysis mechanism. J. Am. Chem. Soc. 144 (2022)

8204–8213.

[79] L. Lin, R. Xin, M. Yuan, T. Wang, J. Li, Y. Xu, X. Xu, M. Li, Y. Du, J. Wang, S. Wang, F. Jiang, W. Wu, C. Lu, B. Huang, Z. Sun, J. Liu, J. He, G. Sun, revealing spin magnetic effect of iron-group layered double hydroxides with enhanced oxygen catalysis. ACS Catal. 13 (2023) 1431–1440.

[80] Y. Zhang, X. Jing, K. Jing, L. Chang, W. Bao, Study on the pore structure and oxygen-containing functional groups devoting to the hydrophilic force of dewatered lignite. Appl. Surf. Sci. 324 (2015) 90–98.

[81] Q. Ye, J. Xu, Y. Zhang, S. Chen, X. Zhan, W. Ni, L. Tsai, T. Jiang, N. Ma, F. Tsai, Metal-organic framework modified hydrophilic polyvinylidene fluoride porous membrane for efficient degerming selective oil/water emulsion separation. NPJ Clean Water 5 (2022) 23.

Figures and Captions:

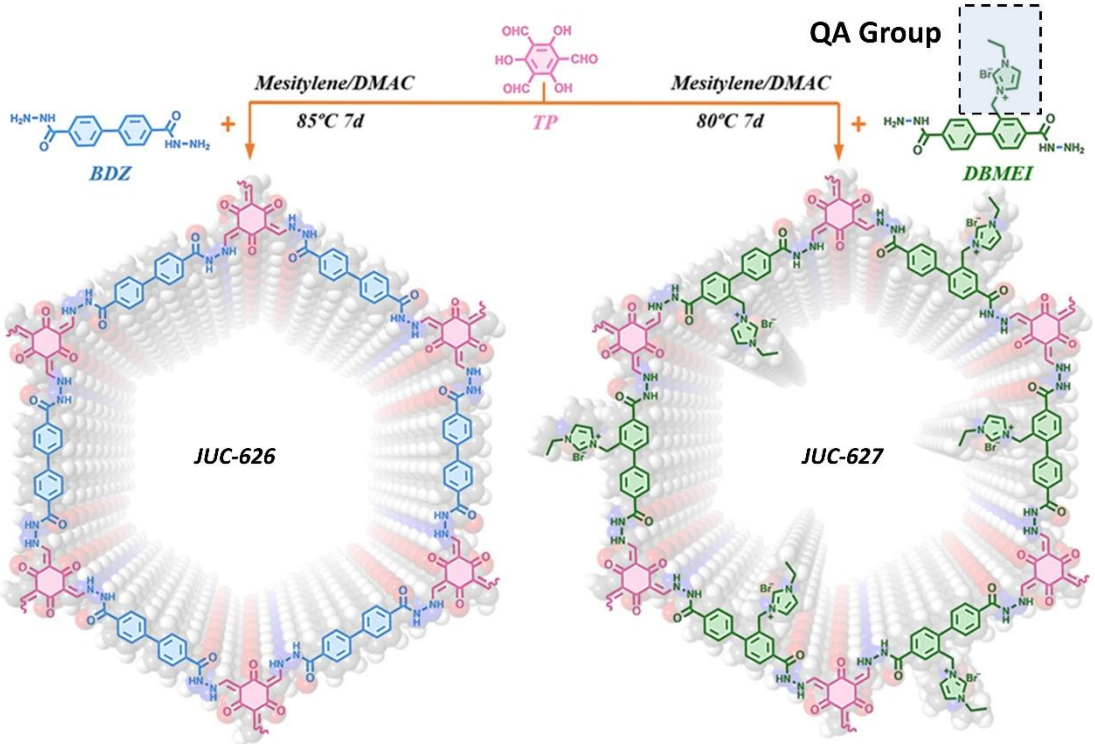

Scheme 1. Syntheses and structures of JUC-626 and JUC-627.

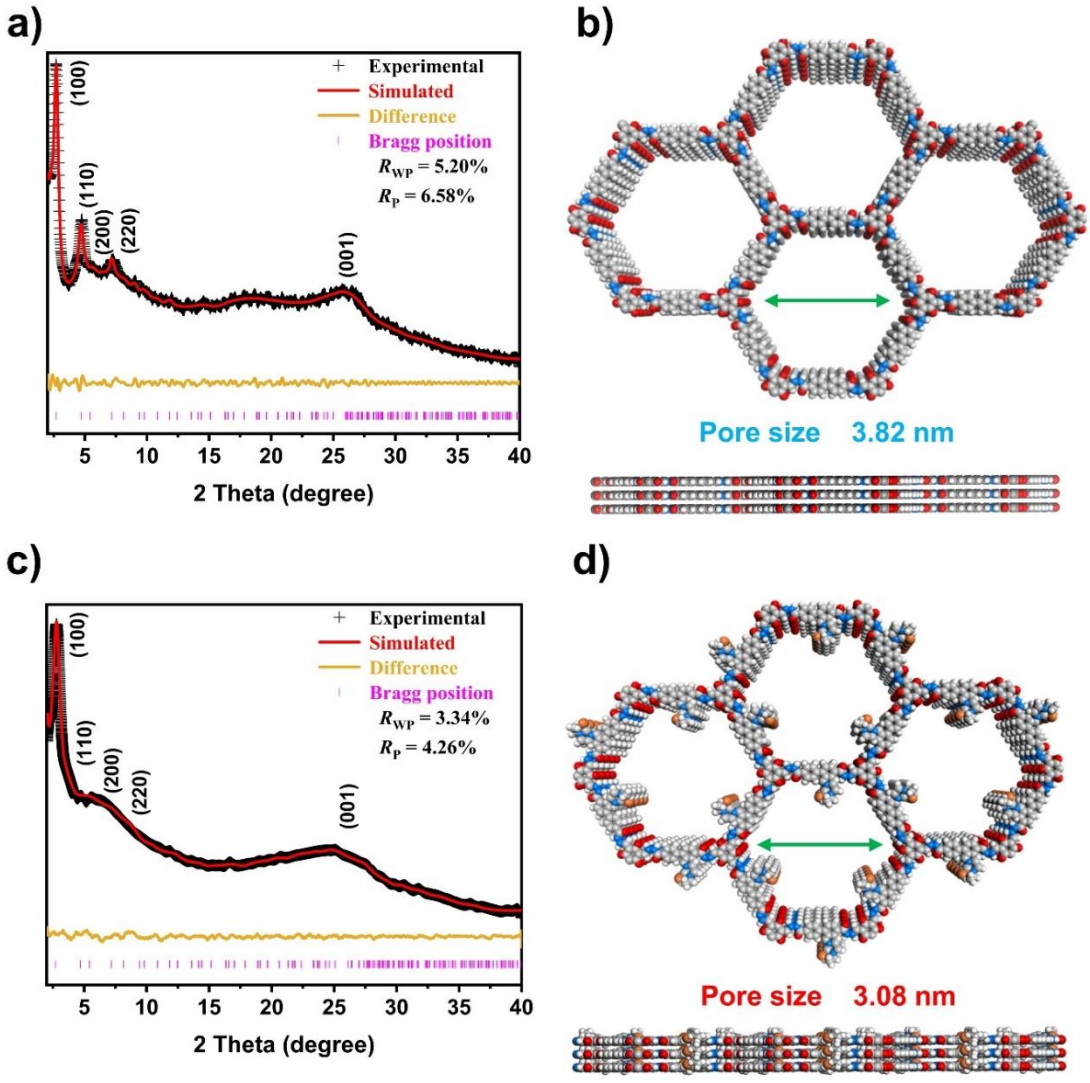

Figure 1. PXRD patterns of (a) JUC-626 and (c) JUC-627. Observed (black), Pawley-refined (red)， difference between observed and refined profiles (yellow) and brag position (pink). Partial structures of JUC-626 (b) and JUC-627 (d) viewed along the *c*-axis and parallel to the *ab* plane (gray, blue, red and white spheres represent C, N, O and H atoms, respectively).

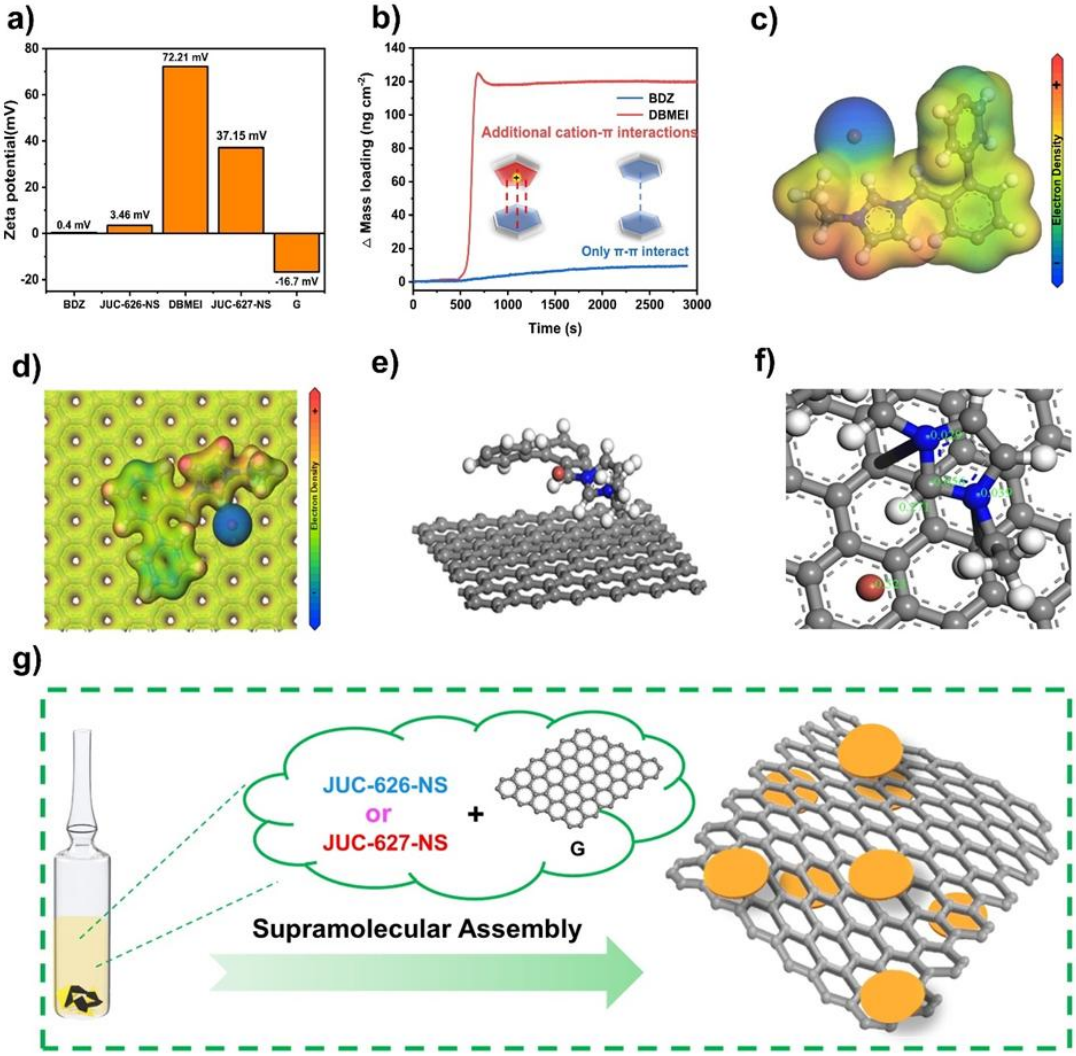

Figure 2. (a) Zeta potential of BDZ, JUC-626-NS, DBMEI, JUC-627-NS and graphene (G). (b) QCM measurement of mass change for model molecules. Inset: Schematic diagram of cation-π interaction and π-π interaction. (c) Electrostatic potential of JUC-627-NS molecular fragment. (d) Electrostatic potential of JUC-627-NS molecular fragment and graphene. (e) Optimized structures of JUC-627-NS molecular fragment and graphene. (f) Crystal orbital overlap population between molecular fragment of JUC-627-NS and graphene.

(g) Synthesis schematic of JUC-626-NS@G-X (X = 1, 2, 3) or JUC-627-NS@G-X (X = 1, 2, 3).

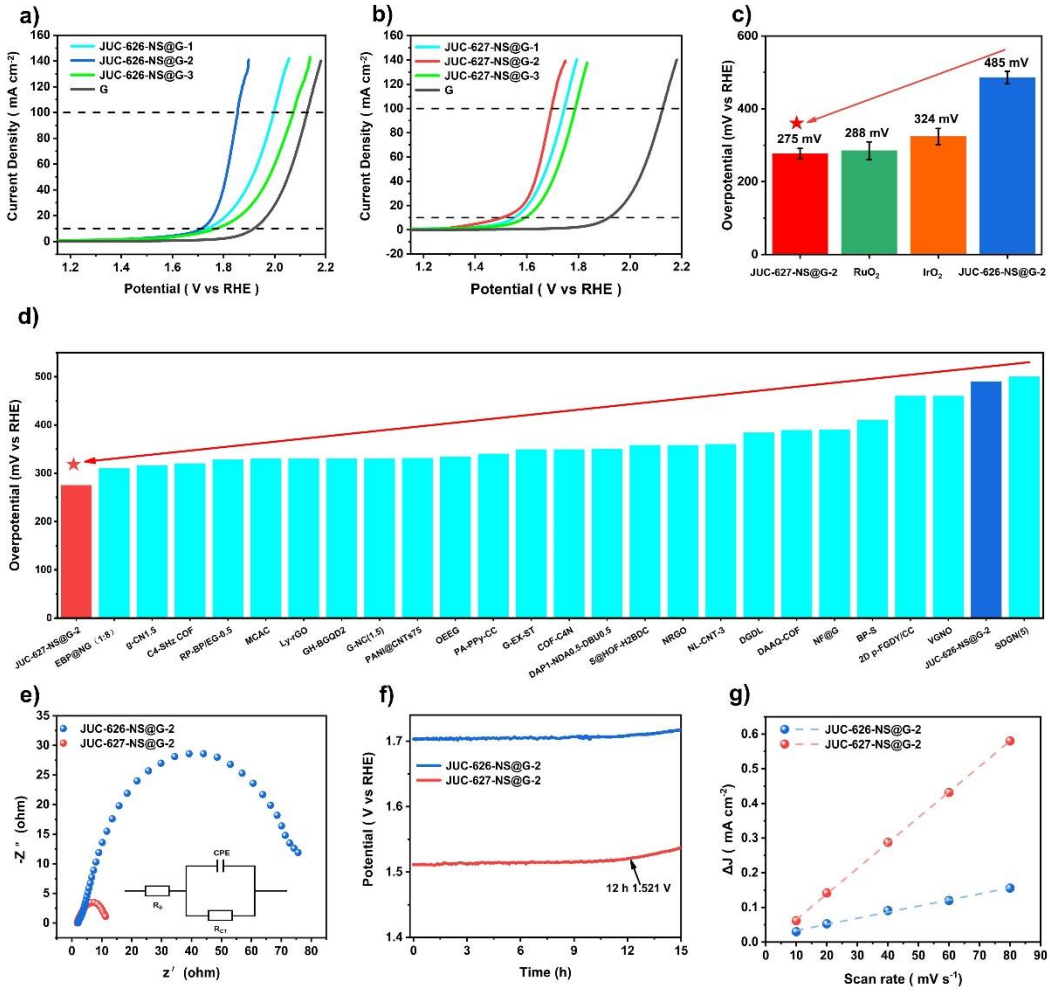

Figure 3. LSV curves of (a) JUC-626-NS@G-X and (b) JUC-627-NS@G-X in O_2-saturated 1 M KOH electrolyte. (c) Comparison of overpotential for the obtained composites with commercial precious metal catalysts. (d) Comparison of overpotential for the obtained composites with the reported metal- and pyrolysis-free catalysts for OER. (e) The impedance for JUC-626-NS@G-2 and JUC-627-NS@G-2. Inset: the equivalent electric circuit. (f) Time-dependent potential curves for JUC-626-NS@G-2 and

JUC-627-NS@G-2 at current density of 10 mA cm^{-2}. (g) Double-layer capacitance (Cdl) measurements of JUC-626-NS@G-2 and JUC-627-NS@G-2.

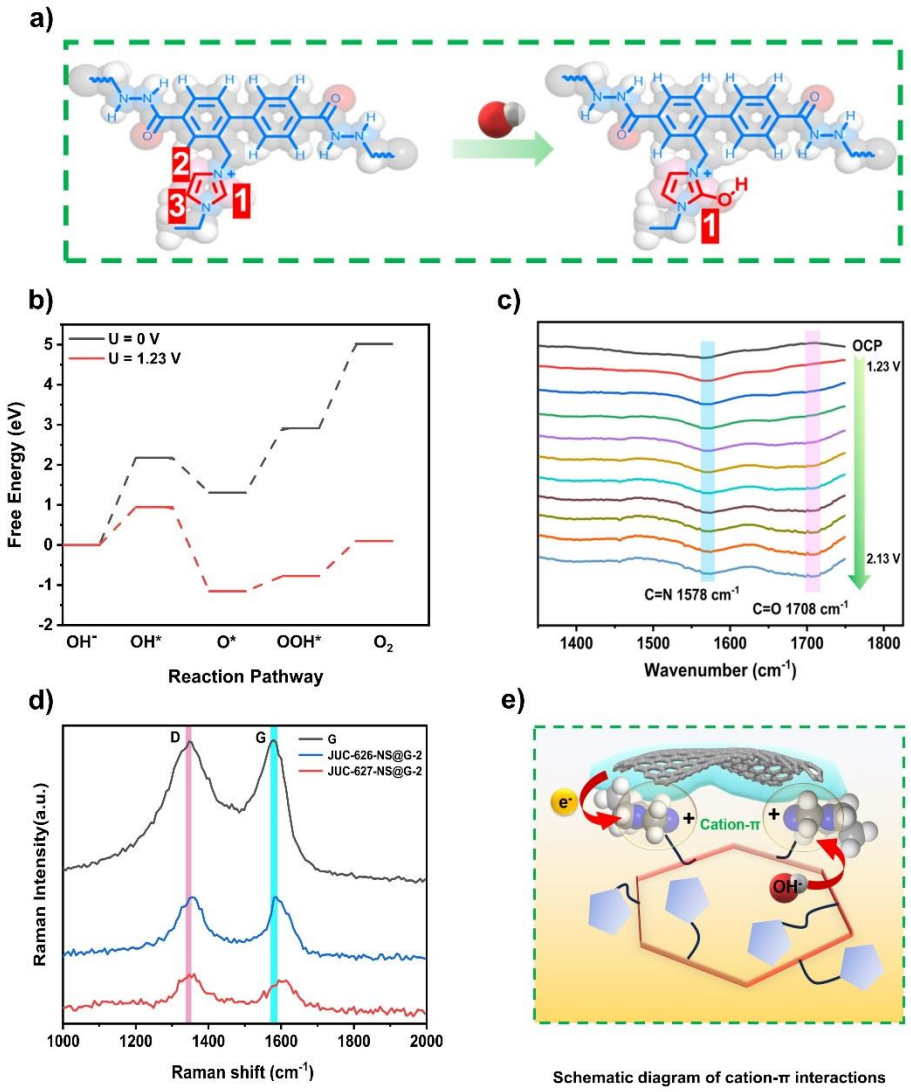

Figure 4. (a) Adsorption of OH^- on C1 atom of JUC-627-NS molecular fragment. (b) Free energy diagram for JUC-627-NS at U = 0 V (black) and U = 1.23 V (red). (c) In-Situ FT-IR spectra of JUC-627-NS at 1.23 V-2.13 V. (d) In-Situ Raman spectra of graphene (G), JUC-626-NS@G-2 and JUC-627-NS@G-2. (e) Schematic diagram of cation-π interactions promoting charge transfer.